

ON THE PHASE DIAGRAM FOR MICROPHASE SEPARATION OF DIBLOCK COPOLYMERS: AN APPROACH VIA A NONLOCAL CAHN–HILLIARD FUNCTIONAL*

RUSTUM CHOKSI[†], MARK A. PELETIER[‡], AND J. F. WILLIAMS[†]

Abstract. We consider analytical and numerical aspects of the phase diagram for microphase separation of diblock copolymers. Our approach is variational and is based upon a density functional theory which entails minimization of a nonlocal Cahn–Hilliard functional. Based upon two parameters which characterize the phase diagram, we give a preliminary analysis of the phase plane. That is, we divide the plane into regions wherein a combination of analysis and numerics is used to describe minimizers. In particular we identify a regime wherein the uniform (disordered state) is the unique global minimizer; a regime wherein the constant state is linearly unstable and where numerical simulations are currently the only tool for characterizing the phase geometry; and a regime of small volume fraction wherein we conjecture that small well-separated approximately spherical objects are the unique global minimizer. For this last regime, we present an asymptotic analysis from the point of view of the energetics which will be complemented by rigorous Γ -convergence results to appear in a subsequent article. For all regimes, we present numerical simulations to support and expand on our findings.

Key words. diblock copolymers, phase diagram, modified Cahn–Hilliard equation

AMS subject classifications. 74N15, 49S05, 35K30, 35K55

DOI. 10.1137/080728809

1. Introduction. A diblock copolymer is a linear-chain molecule consisting of two subchains joined covalently to each other. One of the subchains is made of N_A monomers of type A and the other consists of N_B monomers of type B. Below a critical temperature, even a weak repulsion between unlike monomers A and B induces a strong repulsion between the subchains, causing the subchains to segregate. A macroscopic segregation where the subchains detach from one another cannot occur because the chains are chemically bonded. Rather, a phase separation on a mesoscopic scale with A- and B-rich domains emerges (see Figure 1). The observed mesoscopic domains, illustrated in Figure 2, are highly regular periodic structures including lamellae, spheres, cylindrical tubes, and double gyroids (see, for example, [4, 51, 16, 21]).

The usefulness of block copolymer melts is exactly this remarkable ability for self-assembly into particular geometries. For example, this property can be exploited to create materials with *designer* mechanical, optical, and magnetic properties [4, 21]. Therefore, from a theoretical point of view, one of the main challenges is to predict the phase geometry/morphology for a given set of material parameters (i.e., the creation of the phase diagram). There are three dimensionless material parameters involved in the microphase separation: (i) χ , the *Flory–Huggins interaction parameter* measuring the incompatibility of the two monomers; (ii) $N = N_A + N_B$, the *index of polymerization* measuring the number of monomers per macromolecule; and (iii) f ,

*Received by the editors June 28, 2008; accepted for publication (in revised form) January 8, 2009; published electronically April 1, 2009.

<http://www.siam.org/journals/siap/69-6/72880.html>

[†]Department of Mathematics, Simon Fraser University, Burnaby V5A 1S6, BC, Canada (choksi@math.sfu.ca, jfw@math.sfu.ca). The research of these authors was partially supported by NSERC Canada Discovery grants.

[‡]Department of Mathematics, Eindhoven University of Technology, Eindhoven, The Netherlands (m.a.peletier@tue.nl). This author’s research was partially supported by NWO project 639.032.306.

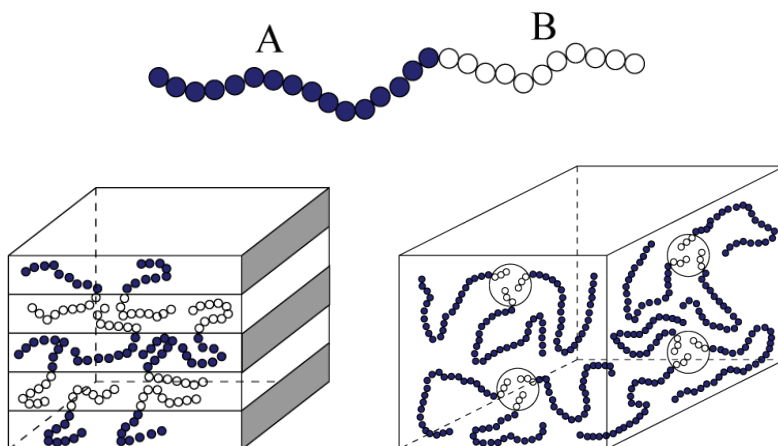


FIG. 1. Top: a diblock copolymer macromolecule. Bottom: microphase separation of diblock copolymers.

the *relative molecular weight* measuring the relative length of the A-monomer chain compared with the length of the whole macromolecule, i.e., $f = N_A/N$. The one relevant dimensional parameter is the Kuhn statistical length, l , which can be thought of as the average monomer space size. We will concern ourselves with a system of diblock copolymers of fixed relative molecular weight f and where the A and B monomers have the same Kuhn statistical length.

In the vast physics literature on block copolymers, the state of the art for theoretically predicting the phase diagram is via the *self-consistent mean field theory* (SCMFT) [26, 16, 42]. Here one *simulates* the interactions of the incompatible A and B monomers via (self-consistent) external fields acting separately on the distinct monomer chains. This transforms the formidable task of integrating contributions to the partition function from many-chain interactions to the computation of the contribution of one polymer in a self-consistent field. An approximation is then used to write the partition function and Gibbs free energy explicitly in terms of *coupled* order parameters—the macroscopic monomer densities and the external fields which *generate them*: The coupling is via a modified diffusion equation derived from the Feynman–Kac integration theory. With the adoption of an *ansatz* (assumed symmetry) for the phase structure with one or two degrees of freedom, and respective basis functions of the Laplacian which share the symmetry, one can then minimize the free energy. Comparing the minimum energies for the different ansatzes yields the phase diagram (cf. [26]). In this mean field theory, where thermal fluctuations are ignored, one finds that the parameter dependence is based solely on the products χN and f . Figure 2(left) shows the results of such a calculation showing the predicted structure for different values of χN and f , while Figure 2(right) enables a comparison with experimental observations for polyisoprene-styrene diblocks by Khandpur et al. [25].

As was shown in [12], linearization of the dependence of the monomer density on the external fields (via the modified diffusion equations) yields a density functional theory, first proposed by Ohta and Kawasaki [30] (see also [28, 29]). This density functional theory entails minimization of a nonlocal Cahn–Hilliard-like free energy defined over one order parameter (the relative monomer difference). Here, the standard Cahn–Hilliard free energy is supplemented with a nonlocal term, reflecting the

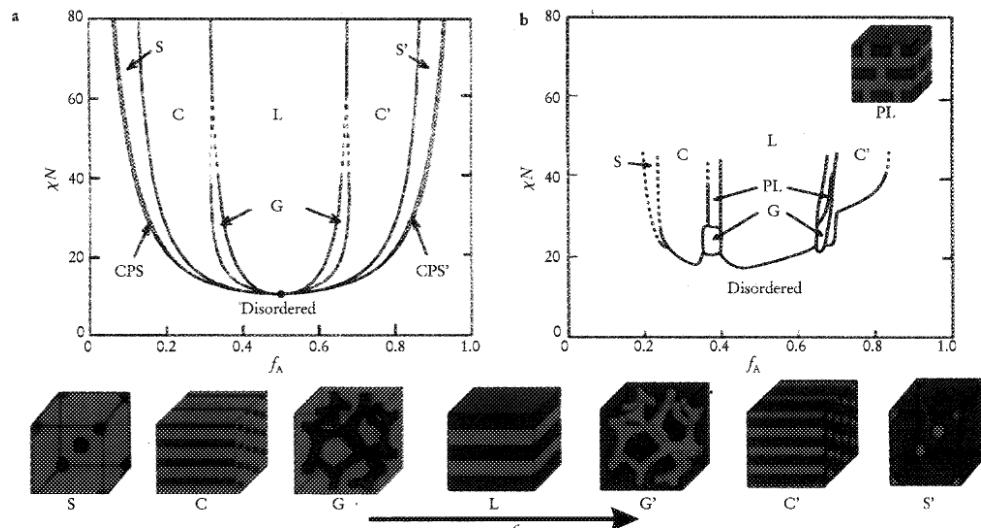


FIG. 2. (a) *SCMFT* phase diagram of Matsen and Schick (cf. [26]) for microphase separation of diblock copolymers: The relative molecular weight f is denoted by f_A and the phases are labeled L for lamellar, G for gyroid, C for hexagonally packed cylinders, S for spheres, and CPS for close packed spheres. (b) Experimental phase diagram for polyisoprene-styrene by Khandpur et al. [25]. PL stands for perforated lamellar. Reprinted with permission from F. S. Bates and G. H. Fredrickson, *Physics Today*, Volume 52, Issue 2, pp. 32–38, 1999. ©1999, American Institute of Physics.

first-order effects of the connectivity of the monomer chains:

$$(1.1) \quad \int_{\Omega} \left(\frac{\varepsilon^2}{2} |\nabla u|^2 + \frac{(1-u^2)^2}{4} \right) dx + \frac{\sigma}{2} \int_{\Omega} \int_{\Omega} G(x, y) (u(x) - m) (u(y) - m) dx dy,$$

where G denotes the Green's function of $-\Delta$ on a cube $\Omega \subset \mathbb{R}^3$ with periodic boundary conditions. Regions where u is approximately equal to 1 (respectively, -1) represent pure A (respectively, B) monomer-rich phases, and thus $m = 2f - 1$. We minimize (1.1) over all u with mass average set to m . We refer to the above functional as a *nonlocal Cahn–Hilliard functional*, but it is also referred to as the *Ohta–Kawasaki functional*.

In this article, our aim is towards an understanding of the phase diagram via minimization of this functional. More precisely, for given values of ε , σ , and m , we minimize the functional over all u , with prescribed mass average m , and focus on characterizing geometrical characteristics of the minimizers as a function of the parameters ε , σ , and m . As a simply nonlocal perturbation to a well-studied problem in the calculus of variations, this is a natural variational problem to consider—independent of any direct application. Indeed, one can simply view the problem as a mathematical paradigm for the modeling of (quasi-)periodic pattern formation, induced by competing short-range (the first two terms) and long-range (the nonlocal term) interactions [41]. Hence, seeking to characterize minimizers (either global or local) for given values of ε , σ , and m is both natural and fundamental.

Nevertheless, our interests are also directly tied to the application to the phase diagram of a diblock copolymer melt. The simplicity of the Ohta–Kawasaki theory is that it entails minimization of a free energy which can be directly studied, both analytically and numerically, without a priori assumptions for the basic symmetry of the minimizing microstructure (which is necessary for simulations of the *SCMFT*).

The vast majority of symmetries which have been considered in the SCMFT are related to known constant mean curvature surfaces (i.e., surfaces with minimal area subject to a volume constraint) which have been experimentally observed in phase boundaries in diblock copolymers [4, 26]. Note that not only does this limit the consideration of structures which have yet to be observed, but actual minimizers in either theory will not, in general, have phase boundaries with exactly constant mean curvature: Because of the connectivity of the monomer chains, one would expect that the phase separation is not determined solely by interfacial energy. While, as we shall see, simulations based upon minimizing (1.1) also suggest minimizers have phase boundaries which resemble constant mean curvature surfaces, one readily sees from (1.1) that the nonlocal term will have an effect on the structure of the phase boundary (see Remark 4.3 and [14]). Surely, this is also the case with the SCMFT.

On the other hand, based upon the approximation and truncations used in the derivation [12], one could, and should, be skeptical as to whether or not the essential physics is preserved in the intermediate to strong segregation regime, where the interface thickness is relatively small. However, we wish to point out that all of the phases which have been (numerically) predicted purely from the SCMFT [26, 52] can be (numerically) generated from the minimization of (1.1), and the latter theory is ansatz-independent (see [47, 48, 46, 53] and section 4.3). Hence, it would seem that one need only keep a rather crude approximation of the polymer A- and B-chain interactions, in order to determine *the basic qualitative geometry*. Three-dimensional simulations for (2.6) were begun by Teramoto and Nishiura in [47, 48] simulating double gyroids and have also been explored in the context of the basic phases and the *Fddd* phase by Yamada et al. in [53, 54]. However, to our knowledge, no thorough phase diagram calculation has been done via the gradient theory approach of (2.6) and, in particular, none within the context of the material parameters χN and f . We emphasize that the latter is crucial in order to make any direct comparison to experiments.

With these comments in mind our long-term program is twofold:

- (i) To explore analytically the extent to which one can describe global minimizers of (1.1) for different regimes of the ε, σ, m parameter space. In particular, what are the natural regimes to consider? When the ground state (global minimizer) is analytically difficult to access (which is indeed the case for the majority of the phase plane), explore the extent to which numerical simulations can be used to describe the general energy landscape of (1.1)—with regard to both local and global minimizers.
- (ii) To explore the extent to which this variational problem can be used to create a phase diagram, which is not only *qualitatively* similar to both the SCMFT phase diagram of [26] (Figure 2, left) and the experimental one (Figure 2, right—see also [25, 40, 21]) but also *quantitatively* similar close to the order-disorder transition. In particular, one must be able to relate all results to the two fundamental parameters χN and f .

The aim of this article is to provide a preliminary step towards these goals. In particular, we identify two parameters $\gamma := 1/(\varepsilon\sqrt{\sigma})$ and m , analogous to χN and f in the SCMFT, which are relevant for the phase diagram. We divide the (m, γ) plane into several regions (see Figure 3).

Region I. In the region defined by $m \in (-1, 1)$ and $\gamma \leq \frac{2}{1-m^2}$, we prove in section 3 that the uniform state (often referred to as the *disordered state*) is the unique global minimizer.

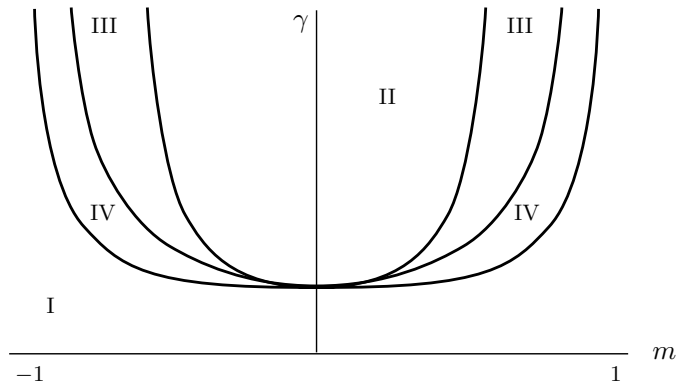


FIG. 3. Rough sketch of regions of the $m \times \gamma$ plane for minimizers of (2.2) on a large domain (cf. Remark 2.1). The bottom curve is $\gamma = \frac{2}{1-m^2}$, below which we prove that the disordered state is the unique global minimizer. The top curve shows the linear stability of the disordered state; that is, for $\gamma > \frac{2}{1-3m^2}$ the disordered state is unstable. The middle curve divides the regime $\frac{2}{1-3m^2} > \gamma > \frac{2}{1-m^2}$ into regions where we find, numerically, that the disordered state is the minimizer (Region IV) and where it is not the minimizer (Region III).

Region II. Section 4 addresses the region defined by $m \in (-1/\sqrt{3}, 1/\sqrt{3})$ and $\gamma \geq \frac{2}{1-3m^2}$, which forms the central part of the phase diagram. It is the region wherein the constant state is linearly unstable (see section 4.1); thus, whatever the global minimizer is, it must have some structure (i.e., not be uniform). In this region one expects to see the basic phase structures of the experimental and SCMFT diagrams of Figure 2: lamellar, cylindrical, spherical, double-gyroid (see section 4.3 for a discussion of the *Fddd* phase). Unfortunately, there is little one can rigorously prove about global minimizers, and even the rigorous study of local minimizers is usually based upon some ansatz. Hence, numerical simulations are currently the only tool to determine geometric properties of the minimizer. While a thorough numerical investigation of Region II is in progress, we give a sample of typical final-state simulations showing lamellar, cylindrical, double-gyroid, and spherical phase patterns. We also find *perforated lamellar* phases similar to those observed in the experiments on polyisoprene-styrene by Khandpur et al. [25].

Regions III and IV. In section 5, we address the remaining region in the (m, γ) -parameter plane, indicated by III and IV in Figure 3. In this region, the constant state is linearly stable; however, a basic scaling argument (presented in section 5.2) shows that small well-separated spheres have lower energy than the constant state for sufficiently large γ . In section 5.1, we present the results of a numerical investigation of the region for $\gamma < 25$. In particular, we determine a transition curve that separates order (Region III) from disorder (Region IV). In section 5.3, we describe analytical support for well-separated spherical phases in Region III via an asymptotic analysis of the energy when m tends to ± 1 . This analysis forms the basis of a rigorous Γ -convergence study currently underway which will appear elsewhere (cf. [10, 11]).

Throughout this article, we will adopt periodic boundary conditions. See Remarks 4.2 and 4.3 for a brief discussion on this choice, the role of the boundary conditions, and other possible choices.

2. The nonlocal Cahn–Hilliard functional and modified Cahn–Hilliard equation. Let $\Omega \subset \mathbb{R}^3$ denote the three-dimensional flat torus of diameter L ; i.e.,

adopting periodic boundary conditions, we may take $\Omega = [-\frac{L}{2}, \frac{L}{2}]^3$. We fix $m \in (-1, 1)$ and minimize (1.1), i.e.,

$$(2.2) \quad E_{\varepsilon, \sigma}(u) := \frac{\varepsilon^2}{2} \int_{\Omega} |\nabla u|^2 dx + \int_{\Omega} \frac{1}{4}(1 - u^2)^2 dx + \frac{\sigma}{2} \int_{\Omega} |\nabla v|^2 dx,$$

over all $u \in \{u \in H^1(\Omega, [-1, 1]) \mid \int_{\Omega} u = m\}$. Here u represents the (macroscopic) relative monomer density (i.e., relative density of the A monomers minus that of the B); ε represents the interfacial thickness (suitably rescaled) at the A and B monomer intersections; and v is related to u via the boundary value problem

$$(2.3) \quad -\Delta v = u - m,$$

with periodic boundary conditions for v on $\partial\Omega$. Note that the last term of (2.2) is the H^{-1} norm squared of the function $u(x) - m$, i.e.,

$$\int_{\Omega} |\nabla v|^2 dx = \int_{\Omega} \int_{\Omega} G(x, y) (u(x) - m) (u(y) - m) dx dy = \|u - m\|_{H^{-1}(\Omega)}^2,$$

where G denotes the Green's function of $-\Delta$ on the torus Ω (see Appendix B for details).

Following [12], one finds that, up to leading order, the quantities ε , σ , and m are related to the dimensionless parameters χN and f as follows:¹

$$(2.4) \quad \varepsilon^2 \sim \frac{l^2}{f(1-f)\chi}, \quad \sigma \sim \frac{1}{f^2(1-f)^2 l^2 \chi N^2}, \quad m = 2f - 1,$$

where l is the Kuhn statistical length. The fundamental product χN is therefore related to σ and ε via

$$(2.5) \quad \chi N \sim \frac{1}{f^{3/2} (1-f)^{3/2} \varepsilon \sqrt{\sigma}}.$$

We assume that the evolution is given by a gradient flow for the free energy (2.2). As we explain in Appendix B, a convenient inner product with respect to which we compute this gradient flow is H^{-1} (the same as for the Cahn–Hilliard equation), and this computation gives the following *modified Cahn–Hilliard equation*: Solve

$$(2.6) \quad \frac{\partial u}{\partial t} = \Delta (-\varepsilon^2 \Delta u - u + u^3) - \sigma(u - m)$$

on the torus Ω . Setting $\sigma = 0$ yields the well-known Cahn–Hilliard equation (or, more precisely, the Cahn–Hilliard equation with constant mobility). Note that the last term comes from the nonlocal term in (2.2): Using the H^{-1} norm as the inner product in computing the gradient reduces the nonlocality to a zeroth-order perturbation of the Cahn–Hilliard equation. As with the Cahn–Hilliard equation, (2.6) preserves the total mass average $\int_{\Omega} u$ of the solution, provided the initial data u_0 satisfies $\int_{\Omega} u_0 = m$. Otherwise, one readily sees that the mass average will adjust to m exponentially fast.

¹Explicit constants inherent in (2.4) and (2.5) are derived in [12]. However, they are based upon the form of the interaction Hamiltonian used for the SCMF. This choice of a first-order interaction Hamiltonian gives rise to a double-well energy of the form

$$W(u) = \begin{cases} \frac{(1-u^2)}{4} & \text{if } |u| \leq 1, \\ +\infty & \text{otherwise,} \end{cases}$$

not $W(u) = 1/4(1 - u^2)^2$ used for (2.2) and (2.6).

2.1. The fundamental dependence on $\varepsilon\sqrt{\sigma}$. For the purposes of determining the phase diagram of (2.2), one can reduce the characterization of phase space to two parameters: $\varepsilon\sqrt{\sigma}$ and m . To see this, we may rescale the functional (2.2) via

$$\tilde{x} = \sqrt{\sigma} x, \quad \tilde{\Omega} = \sqrt{\sigma} \Omega, \quad \tilde{\varepsilon} = \varepsilon \sqrt{\sigma},$$

to find

$$(2.7) \quad \tilde{\varepsilon}^2 \int_{\tilde{\Omega}} |\nabla_{\tilde{x}} u|^2 d\tilde{x} + \int_{\tilde{\Omega}} \frac{1}{4} (1 - u^2)^2 d\tilde{x} + \int_{\tilde{\Omega}} |\nabla_{\tilde{x}} \tilde{v}|^2 d\tilde{x},$$

where \tilde{v} solves

$$-\Delta_{\tilde{x}} \tilde{v} = u - m \quad \text{on } \tilde{\Omega}.$$

Equivalently, we may rescale (2.6) as follows:

$$\tilde{u} = u - m, \quad \tilde{x} = \sqrt{\sigma} x, \quad \tilde{L} = \sqrt{\sigma} L, \quad \tilde{t} = \sigma t, \quad \tilde{\varepsilon} = \varepsilon \sqrt{\sigma}.$$

This leads to

$$(2.8) \quad \frac{\partial \tilde{u}}{\partial \tilde{t}} = -\tilde{\varepsilon}^2 \Delta_{\tilde{x}}^2 \tilde{u} + \Delta_{\tilde{x}} (\tilde{u}^3 + 3m\tilde{u}^2 - (1 - 3m^2)\tilde{u}) - \tilde{u},$$

solved on the torus $\tilde{\Omega} = [-\frac{\tilde{L}}{2}, \frac{\tilde{L}}{2}]^3$.

One can also recognize the sole dependence on $\tilde{\varepsilon}$ in the basic scaling laws associated with minimizers of (2.2) outside the weak segregation regime (i.e., when the interfacial boundary thickness is sufficiently small). To this end we fix a value of $m \in (-1, 1)$ and focus on scalings in ε and σ . Following [8], the minimum energy (per unit volume) associated with (2.2) scales like $\varepsilon^{2/3} \sigma^{1/3} = (\varepsilon\sqrt{\sigma})^{2/3}$. On the other hand, one can, at least formally (rigorously in dimension $n = 1$; cf. [27]), see that there are two length scales for minimizers: an *intrinsic length* for the phase patterns of order $(\frac{\varepsilon}{\sigma})^{1/3}$, and an *interfacial thickness* of order ε . It is the ratio of these length scales which controls the degree of the phase separation, i.e.,

$$(2.9) \quad \left(\frac{\varepsilon}{\sigma}\right)^{1/3} \varepsilon^{-1} = \frac{1}{(\varepsilon\sqrt{\sigma})^{2/3}}.$$

Here again the combination $\varepsilon\sqrt{\sigma}$ emerges.

Since the relevant regimes are for small $\tilde{\varepsilon}$, we introduce the parameter

$$\gamma := \frac{1}{\tilde{\varepsilon}} = \frac{1}{\varepsilon\sqrt{\sigma}}.$$

Note that according to (2.4) and (2.5), we have $\gamma \sim \chi N$.

Remark 2.1. Let us provide a few comments on the role of the domain size L (respectively, \tilde{L}). Minimizers of (2.2) or (2.7) possess an intrinsic length scale which is independent of the domain size L (respectively, \tilde{L}). This of course is assuming the domain size is much larger than this intrinsic length which scales like $(\frac{\varepsilon}{\sigma})^{1/3}$ for (2.2) and $\tilde{\varepsilon}^{1/3}$ for (2.7). Note that

$$\tilde{\varepsilon}^{1/3} = \sqrt{\sigma} \left(\frac{\varepsilon}{\sigma}\right)^{1/3}$$

for (2.7). As for the precise nature of the geometry, numerics suggest that for L sufficiently large, the effect on the geometry of the phase boundary is minimal (see further section 4.3 and Remark 4.3). Thus, we will take the point of view that for the purposes of determining the geometry of the minimizing structure, the role of L is *negligible* as long as it is *sufficiently large*. However, this is not to say that in performing numerics on the gradient flow (2.6) or (2.8) across the phase plane the choice of domain size does not warrant careful attention—see section 4.3.

3. Region I: A rigorous result for disorder. From Figure 2 one might expect that when m is close to ± 1 and/or σ is large (i.e. γ is small), then $u \equiv m$ is a global minimizer of (2.2). This constant state is often referred to as the *disordered* state. We have the following sufficient condition for disorder which holds in any space dimension and for any L .

THEOREM 3.1. *For any $m \in (-1, 1)$, the constant state $u \equiv m$ is the unique global minimizer of (2.2) if*

$$(3.10) \quad 1 - m^2 \leq 2 \varepsilon \sqrt{\sigma} \quad \text{or} \quad \gamma \leq \frac{2}{1 - m^2}.$$

Proof. Setting $W(u) = (1 - u^2)^2/4$, choose $c(m) > 0$ such that for $u \in [-1, 1]$,

$$W(u) \geq \tilde{W}(u) := W(m) + W'(m)(u - m) - \frac{c(m)}{2}(u - m)^2.$$

Letting $E(u)$ denote the energy in (2.2), we have for any $u \in H^1(\Omega, [-1, 1])$ with $\int_{\Omega} u = m$,

$$(3.11) \quad \begin{aligned} E(u) &\geq W(m)L^n + \frac{\varepsilon^2}{2} \int_{\Omega} |\nabla u|^2 dx - \frac{c(m)}{2} \int_{\Omega} (u - m)^2 dx + \frac{\sigma}{2} \int_{\Omega} |\nabla v|^2 dx \\ &= W(m)L^n + \sum_{|\mathbf{k}| \neq 0} \left(\frac{\varepsilon^2}{2} \frac{|2\pi \mathbf{k}|^2}{L^2} - \frac{c(m)}{2} + \frac{\sigma}{2} \frac{L^2}{|2\pi \mathbf{k}|^2} \right) |\hat{u}_{\mathbf{k}}|^2, \end{aligned}$$

where for $\mathbf{k} \in \mathbf{Z}^3$, $\hat{u}_{\mathbf{k}}$ are the Fourier coefficients for u on the cube $\Omega = [-\frac{L}{2}, \frac{L}{2}]^3$ with respect to normalized basis functions. The sum on the right-hand side of (3.11) is positive if

$$(3.12) \quad \frac{\varepsilon^2}{2} \frac{|2\pi \mathbf{k}|^2}{L^2} - \frac{c(m)}{2} + \frac{\sigma}{2} \frac{L^2}{|2\pi \mathbf{k}|^2} \geq 0$$

for all $|\mathbf{k}| = 1, 2, \dots$. Minimizing this expression with respect to $|\mathbf{k}|^2$ (treating it as a continuous variable), we find

$$|\mathbf{k}|^4 = \frac{\sigma L^4}{\varepsilon^2 (2\pi)^4},$$

and hence (3.12) holds if

$$c(m) \leq 2 \varepsilon \sqrt{\sigma}.$$

In this case, the constant state $u \equiv m$ is the unique global minimizer. One readily checks (see Figure 4) that the *optimal* choice of $c(m)$ is

$$c(m) = 1 - m^2. \quad \square$$

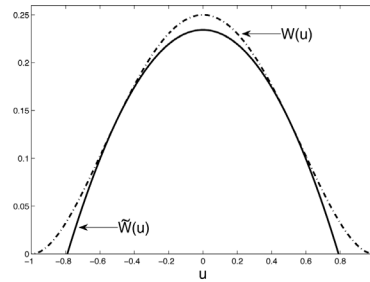


FIG. 4. Plot of $W(u)$ and $\tilde{W}(u)$ for $m = 0.5$.

We note that this argument fails for the pure Cahn–Hilliard case ($\sigma = 0$); in particular, the sample size L will not scale out. However, it is certainly not optimal (except at $m = 0$): Numerical results in section 5.1 indicate that the true order-disorder transition lies strictly above the curve $\gamma = 2/(1 - m^2)$. These numerical results will be used to define the interface between Regions III and IV of Figure 3.

4. Region II: Linear instability of the constant state and simulations.

4.1. Linear instability of the constant state. Following the rescalings of section 2.1, we examine the linear stability of the constant state $u \equiv m$ for (2.6). Linearizing (2.8) about the homogeneous solution $\tilde{u} \equiv 0$ gives

$$\frac{\partial w}{\partial t} = \mathcal{L}w := -\tilde{\varepsilon}^2 \tilde{\Delta}^2 w - (1 - 3m^2) \tilde{\Delta} w - w.$$

Substituting the ansatz

$$w = e^{\lambda t + ik \cdot x},$$

one finds

$$\lambda = -\tilde{\varepsilon}^2 |k|^4 + (1 - 3m^2) |k|^2 - 1.$$

Hence one finds positive values of λ if

$$(4.13) \quad 1 - 3m^2 > 0 \quad \text{or} \quad |m| < \frac{1}{\sqrt{3}} \quad (0.215 < f < 0.785)$$

and, moreover, if

$$(4.14) \quad (1 - 3m^2)^2 > 4\tilde{\varepsilon}^2 \quad \text{or} \quad (1 - 3m^2) > 2\varepsilon\sqrt{\sigma}.$$

Thus in terms of γ , we find the boundary of linear stability to be

$$(4.15) \quad \gamma = \frac{2}{1 - 3m^2}.$$

4.2. Rigorous results. It is natural to seek rigorous results on the structure of a global minimizer of (2.2) in Region II. Sadly, very little can be proven in dimension three. Heuristically, one expects the competition between the first two terms of (2.2) and the nonlocal term to result in a periodic-like structure with an intrinsic scale determined entirely by ε and σ . Within a period cell, a phase boundary of approximate

width ε would have a geometry close to being area-minimizing (the effect of the first two terms in (2.2)). As we shall see, numerical simulations confirm these heuristics.

The periodicity of minimizers is the focus of [3]. Here one considers the sharp interface version of (2.2), wherein the interfacial thickness is sent to zero in relation to σ such that the size of the intrinsic length scale remains positive. The periodicity and intrinsic length scale are addressed by proving weaker statements on the spatial uniformity of the energy distribution of minimizers. While hardly optimal, these results confirm that global minimizers must possess a certain uniformity of structure with respect to the intrinsic length scale. In [43], the methods of [3] have recently been expanded to produce analogous results for minimizers of the full functional (2.2).

The study of *local minimizers* is perhaps more tractable. In a series of papers (for example, [32, 33, 34, 35, 36]) Ren and Wei study the spectral stability of certain ansatzes—lamellae, spheres, cylinders. For the latter two, they work within a radially symmetric domain. Interestingly, they are also able to prove the stability of certain *wriggled* lamellar and circular structures. However interesting, these results are not easily tied to fixed values of the parameters, and, in particular, it is difficult to address which of the geometries has the lowest energy. Work, in a similar spirit, but with different techniques in two dimensions, has recently been carried out in [7]. In [13], a full global treatment is given for the second variation of the sharp interface version of (2.2). The formula is then applied to some simple ansatzes.

To further emphasize the difficulty of characterizing global or local minimizers, note that, even if one imposes periodicity on admissible patterns as a hard constraint reflecting the effect of the nonlocal term and considers the remaining *perimeter* problems, one is still confronted with fundamental difficulties. Indeed, this reduction leads to *the periodic Cahn–Hilliard and isoperimetric problems* for which many questions remain open in three space dimensions [14, 37, 38].

4.3. Simulations. The most feasible approach for characterizing global or even local minimizers in Region II is via numerical simulations of (2.6). Here we present some representative steady state simulations starting from random initial data, which depict all the phases observed in both the SCMFT and experimental studies summarized in Figure 2. They are presented in Figure 5, where we show the $u = m$ level sets of the steady state simulations. Figure 5 shows typical solutions for a variety of parameter values. In particular, we have stripes, cylinders, perforated lamellae, double gyroids, and spheres. We give two more illustrative views of the double-gyroid simulation in Figures 6(a) and (b), where for the purpose of visualization, we have shown several period cells and slightly modified the choice of level set. The perforated lamellae for $m = 0.45$, $\gamma = 10$ and $m = 0.5$, $\gamma = 20$ are structurally very similar and are presented from different perspectives. The perforated lamellar phase was observed in experiments on polyisoprene-styrene by Khandpur et al. [25] and consists of lamellar layers with orthogonal perforations of tubes. We give two more illustrative views of the perforated lamellar simulation in Figures 6(c) and (d). Note that we have also included spherical simulations outside of Region II ($m = 0.5$, $\gamma = 5$ and $m = 0.7$, $\gamma = 20$). In fact they lie in Region III, which will be the focus of section 5.

One phase which we have yet to capture is the so-called *Fddd* phase (an interconnected orthorhombic network with space group 70) which is distinct from the perforated lamellar phase [52, 53, 45]. Recently, the SCMFT has been used to show that this phase is stable (i.e., energy minimizing amongst the competitors) in a small parameter region [52]. It has also been captured by PDE simulations, similar to (2.6), in [53].

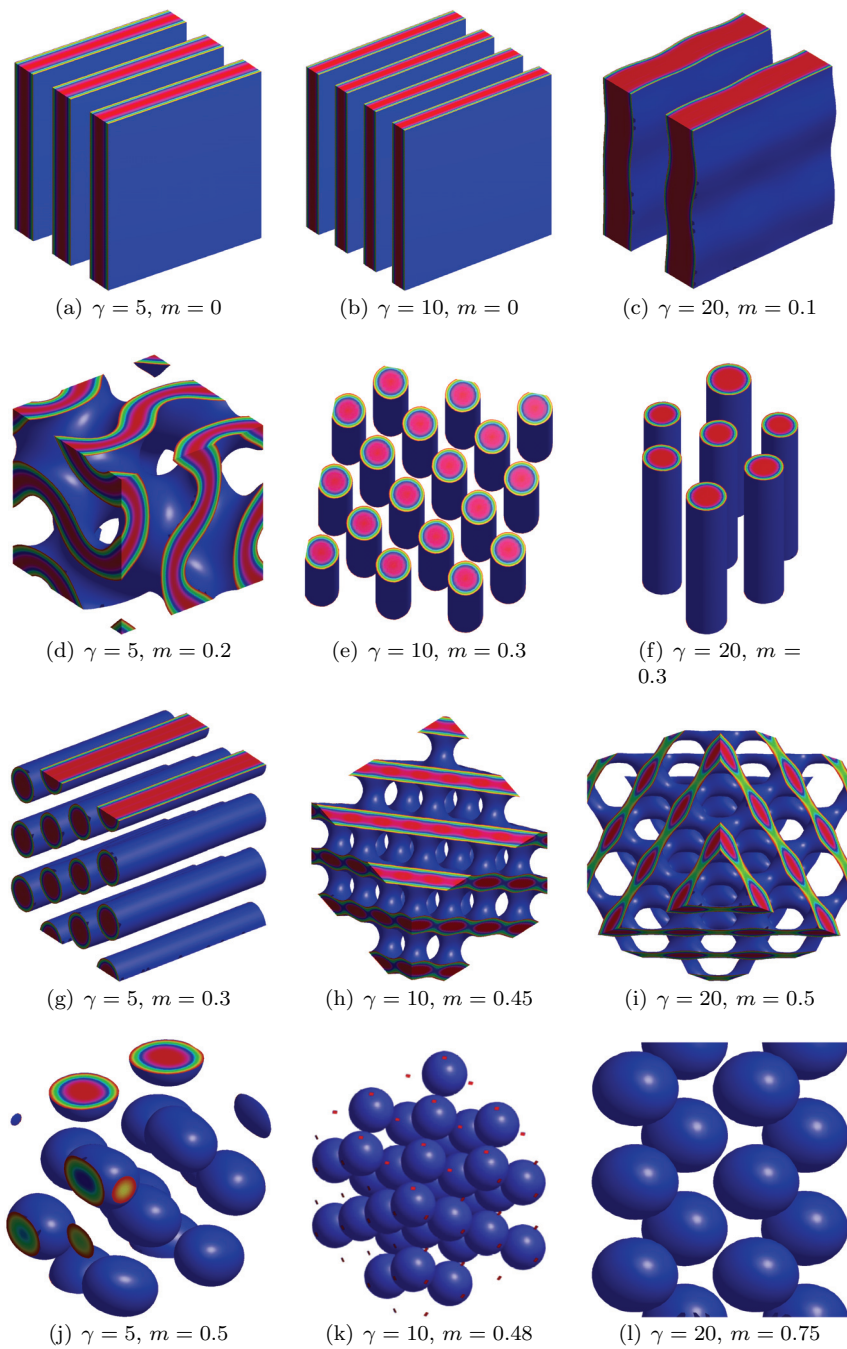


FIG. 5. The $u = m$ level sets of steady state simulations of (2.6) with random initial data. In all cases we have chosen $\varepsilon = 0.04$ and taken $L = \pi/2$ on the left and $L = \pi$ for the other two columns.

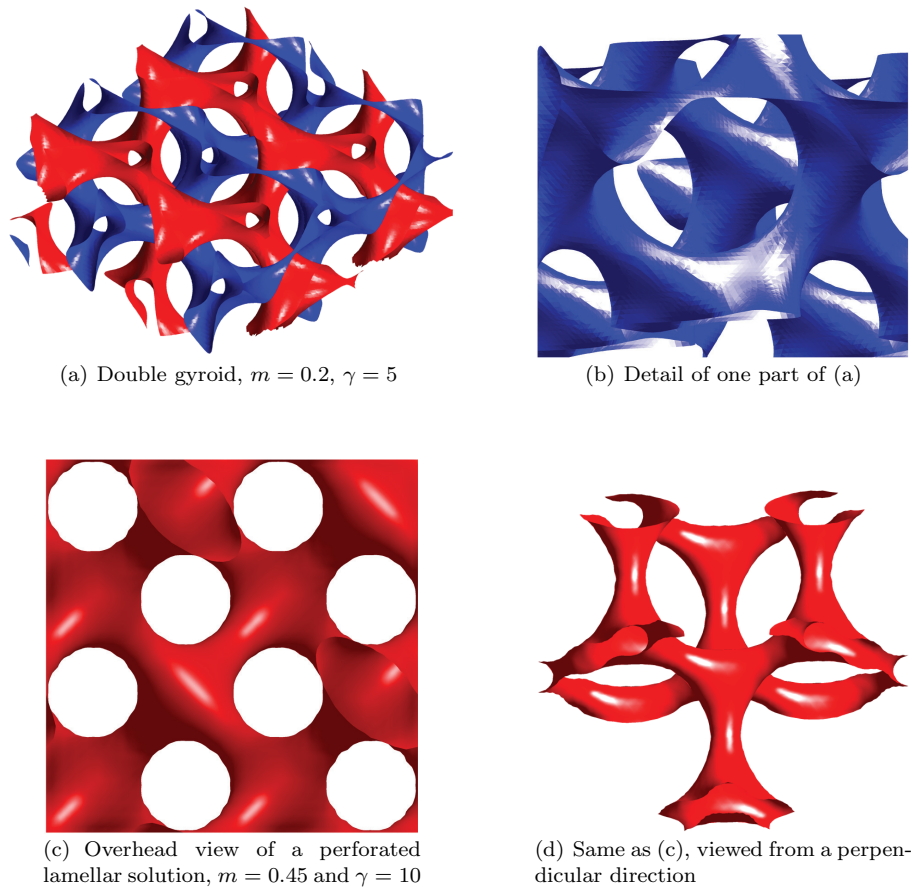


FIG. 6. Views of double-gyroid and perforated lamellar solutions.

It is important to stress that all numerical simulations outside of Region I can be considered only as potentially *locally stable* or even *metastable* states. Solutions to the one-dimensional Cahn–Hilliard equation are known to show metastability where the linearized evolutionary operator about stripe-like profiles can have unstable eigenvalues of size $O(e^{-c/\varepsilon})$ [44]. This means that transient solutions can appear stationary for times $O(e^{c/\varepsilon})$. Figure 5 has two solutions not expected to be minimizers: In $(0.3, 20)$, not all the cylinders are of uniform size, and in $(0.1, 20)$, we expect the oscillations in the stripes with $\gamma = 20$ to eventually diminish.

We also note that, in order to capture fully the symmetry of the phase boundary, one needs to take L sufficiently large. For example, because of finite-size effects the array of cylinders for $\gamma = 10$ is on a rectangular rather than hexagonal grid which we believe to be generic. This is also the case for the perforated lamellae of Figure 6(c), where we expect a hexagonal configuration of the connecting tubes, and for all the spherical simulations for which we expect *BCC* symmetry.

We also performed experiments for the same parameters but different initial data (or several runs with random initial data). For certain parameters, we found different steady state configurations for different initial data—for example, both single and

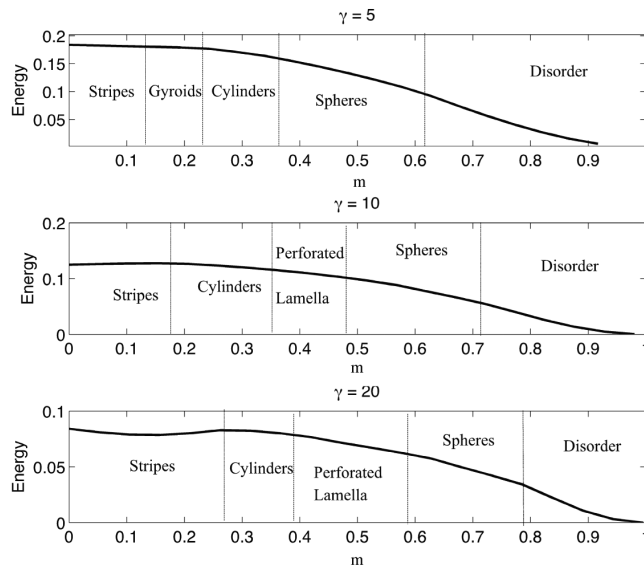


FIG. 7. Energy of stationary profiles as a function of m for $\gamma = 5$ (top), 10 (middle), and 20 (bottom). The dashed lines are preliminary estimates of the phase boundaries.

double gyroids. In this case, a comparison of the free energies was made and the minimizer chosen—for example, the double gyroid had lower energy than the single gyroid. We summarize our steady state simulations throughout Region II (and III) in Figure 7, where we plot the energy of the final stationary states as a function of m for various values of γ . These phase boundaries should be regarded only as rough estimates (see section 6 for further comments). A full phase diagram based upon simulations of the phase boundary is in progress. Here one will perform detailed calculations of certain geometric characteristics like the Euler characteristic [1, 46] and pay careful attention to choosing the sample size L sufficiently large so as to capture the true symmetries of the steady state structures.

A detailed phase diagram starting purely from random initial data requires considerable computational time. The PDE is numerically stiff in time, has spatial structures varying over many orders of magnitude, and exhibits metastability where clearly nonoptimal structures can persist for long times. To overcome some of these issues we typically employed some form of *simulated annealing* by adding random noise or by taking occasional large steps based on linearization of the current profile. Because of the size and nonlinearity of the problem direct minimization algorithms proved infeasible.

One would ideally compute a phase diagram which is not only *qualitatively* similar to both the SCMFT phase diagram of [26] (Figure 2, left) and the experimental one (Figure 2, right—see also [25, 40, 21]) but also *quantitatively* similar, at least close to the order-disorder transition. In particular, one must be able to exactly relate values of γ, m to a value for χN . This requires a calibration of the constant implicit in (2.5), for example, by fitting the order-disorder transitions in $m \times \gamma$ space to match either SCMFT calculations or experimental data.

We conclude this section with a few important remarks.

Remark 4.1. Let us be a bit more specific as to what we mean by the *gyroid* and *double gyroid*. The minimal surface gyroid dates back to Alan Schoen in 1970

[23]. This triply periodic surface with triple junctions has constant mean curvature analogues for a variety of volume fractions [23, 18, 19, 20]. The bicontinuous double gyroid consists of two separate single gyroid networks and has a symmetry associated with space group $Ia\bar{3}d$, whereas the single gyroid is associated with subgroup $I4_132$ [19]. Both surfaces can be viewed on the website of *the Scientific Graphics Project* [49], where one can also find explicit characterizations in terms of level sets of elementary functions, in fact, eigenfunctions of the Laplacian. At this preliminary stage, our basis for claiming that certain of our steady state simulations yield gyroids is twofold: (i) they visually resemble these surfaces; (ii) for the appropriate parameters, we also performed runs where we set as initial conditions the actual gyroids and double gyroids [49] and saw little change in the *topological* nature of the final states.

Remark 4.2. The previous remark and, in fact, all the phases we have noted are directly related to constant mean curvature surfaces. It is important to note that interfaces associated with minimizers of (2.2) will not, in general, have exactly constant mean curvature: Even in the small volume fraction regime, one will not have exactly spherical domains. This is simply due to the effect of the nonlocal term, whose effect on the phase boundary can be seen via the sharp interface version of (2.2) and the consequences of the vanishing first variation and the positive second variation (cf. [14]). Numerics, however, certainly suggest that this perturbation from CMC is very small.

Remark 4.3. Let us further elaborate here on the boundary conditions. Taking the physical domain to be the torus is convenient but perhaps also misleading: The resulting self-imposed periodicity is not the periodicity we wish to capture in self-assembly structures of block copolymers. For instance, on a sufficiently small domain one may find a rectangular rather than hexagonal packing despite its higher energy. The competition of the terms in the energy sets an *intrinsic* length scale for minimizing structures, and it is periodic phase separation on this scale that we wish to model. If we were to work on an arbitrary domain which was sufficiently large with respect to this intrinsic scale and adopted (say) Neumann boundary conditions, we would still expect similar periodic-like structures far away from the boundary. On the other hand, general boundary conditions will most probably effect the exact nature of the phase boundaries. This was previously alluded to in regard to the effect of the nonlocal term on the phase boundary in the case working on a finite torus, and as in this case, one would expect that away from the boundary this effect is small (with respect to the overriding symmetry properties). Thus, one might very well observe *gyroid-like* structures away from the boundary in the case of an arbitrary domain. It would be interesting to investigate this numerically with, for example, finite element methods on general domains.

5. Regions III and IV.

5.1. Numerical calculations of the Region III/IV (order-disorder) boundary. We now focus on the part of the phase plane defined by

$$\left\{ (m, \gamma) \mid 1 > |m| \geq \frac{1}{\sqrt{3}} \right\}$$

and

$$\left\{ (m, \gamma) \mid |m| < \frac{1}{\sqrt{3}} \text{ and } \frac{2}{(1-m^2)} < \gamma < \frac{2}{(1-3m^2)} \right\}.$$

For these parameters, the constant state is linearly stable; however, as we shall see in sections 5.2 and 5.3, a simple scaling argument and an asymptotic analysis of the energy lead one to the conclusion that small (well-separated) spherical structures have lower energy than the constant state. First, we numerically determine the transition from order to disorder, defining Regions III and IV. In the numerical experiments starting from random initial conditions, we typically set $L = \pi$, used $N = 64$ Fourier modes, and took $\Delta t = .001$. Figure 8 presents the bifurcation diagram for the region $m \in (0, 1)$, $\gamma \in (2, 25)$ showing the different solution regions. To estimate the curve separating Regions III and IV we proceeded as follows. An initial regular array was performed from which the curve was estimated. New points were then added near the predicted curve and it was recomputed. We repeated this procedure until the curve could be reliably estimated. For this experiment, the initial data were evolved until either the energy was lower than the disordered state or the solution was sufficiently close to the disordered state. From the basis of our numerical experiments, we conjecture that in Region IV, the constant state is the unique global minimizer: In particular, the Region I/IV interface is artificial and the numerically computed boundary of Figure 8 reflects the true order-disorder transition (ODT) curve.

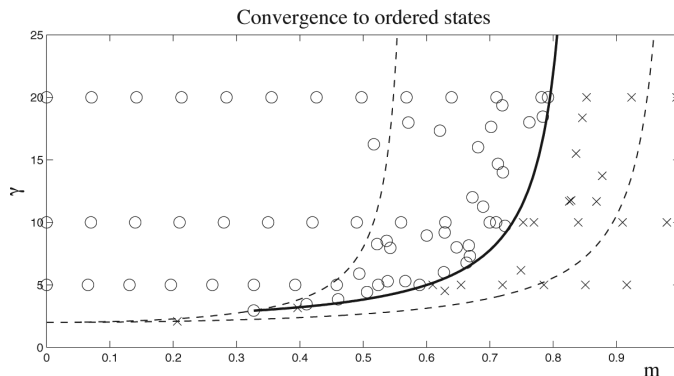


FIG. 8. Numerical bifurcation diagram in three dimensions. The o's indicate runs which converged to states with lower energy than the disordered state. The x's mark simulations which tended to the disordered profile. The solid line marks the best fit separating these regions. The top and lower curves are $\gamma = \frac{2}{1-3m^2}$ and $\gamma = \frac{2}{1-m^2}$, respectively.

5.2. Scaling argument for order. We showed in (4.15) that the regime of $|m| > 1/\sqrt{3}$ gave rise to local stability of the constant, disordered state. However, for very small $1 - |m|$ and the strong segregation regime (small $\varepsilon\sqrt{\sigma}$ or large χN), a simple scaling argument shows that one can have phases of small spheres with lower energy. Here and in the next section, we are interested in a regime of large γ , with m close to -1 , wherein the number of spheres remains $O(1)$. To this end, we will need an asymptotic expansion of the nonlocal energy (i.e., the last term in (1.1) or (2.2)) related to a periodic array of N very small balls of total mass fraction $1/2(1 + m)$ (see Figure 9) in the limit where m tends to -1 and N is fixed. Let $F(x)$ correspond to a periodic array of cubes/squares of size l consisting of a central sphere/disc of diameter a (i.e., $F = 1$ inside the small spheres and -1 outside)—see Figure 9. Then

$$\left\| F - \fint_{\Omega} F \right\|_{H^{-1}(\Omega)}^2 = N \left\| F - \fint_{[0,l]^3} F \right\|_{H^{-1}([0,l]^3)}^2 \sim N \left\| g - \fint_{[0,l]^3} g \right\|_{H^{-1}([0,l]^3)}^2,$$

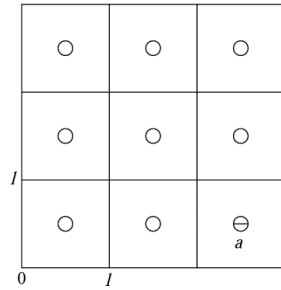


FIG. 9. Periodic array of small spheres of diameter a .

where g defined on one cell $[0, l]^3$ is the analogue of F with the sphere of diameter a replaced with a cube of side length a (see Figure 13).

PROPOSITION 5.1. *There exists a constant C such that*

$$\left\| g - \fint_{[0,l]^3} g \right\|_{H^{-1}([0,l]^3)}^2 \leq C a^5.$$

The proof is standard, but for completeness we present it in Appendix B.²

Turning now to the energy scalings, we assume an ansatz structure of a periodic array of N small balls of total mass fraction m (see Figure 9) with very narrow interfaces of width ε . We compute the energy with respect to the leading order in ε, σ and volume fraction $f = (m + 1)/2$ and then compare with the energy of the uniform state. We consider a cubic domain Ω consisting of N cells of size l ; hence $|\Omega| = N l^3$ and $f = a^3/l^3$. Here we are not interested in constants and make the standard assumption (cf. [6]) that for ε small, we may replace

$$\frac{\varepsilon^2}{2} \int_{\Omega} |\nabla u|^2 dx + \int_{\Omega} \frac{1}{4} (1 - u^2)^2 dx$$

with ε times the perimeter of the interfaces. We compute the energy (2.2) of such a structure:

$$\begin{aligned} E(a, f) &\sim \varepsilon N a^2 + \sigma N a^5 \\ &\sim |\Omega| f \left(\frac{\varepsilon}{a} + \sigma a^2 \right). \end{aligned}$$

Optimizing in a , we find

$$a_{opt} \sim \left(\frac{\varepsilon}{\sigma} \right)^{1/3} \quad \text{and hence} \quad \frac{E(a_{opt}, f)}{|\Omega| f} \sim \varepsilon^{2/3} \sigma^{1/3}.$$

On the other hand, the uniform state $u \equiv m = 2f - 1$ satisfies

$$\frac{E(m)}{|\Omega| f} = \frac{1}{|\Omega| f} \int_{\Omega} W(u) dx \sim f.$$

²In two dimensions one has

$$\left\| g - \fint_{[0,l]^2} g \right\|_{H^{-1}([0,l]^2)}^2 \leq C a^4 \log(l/a).$$

Hence for γ sufficiently large, a periodic array of well-separated small sphere-like patterns has lower energy than the uniform state.

5.3. Asymptotic analysis of the energy in Region III. The scaling analysis of the previous subsection suggests that far up in Region III, small periodic arrangements of spheres (i.e., the spherical phase) have lower energy than the constant state. It is natural to explore this regime from the asymptotics of the energy. That is, we consider a limit wherein $\gamma \rightarrow \infty$ and $f \rightarrow 0$ while keeping the number of phases, loosely referred to as *particles*, $O(1)$, and derive first- and second-order *effective* energies whose energy landscapes are simpler and more transparent. These effective energies are defined over Dirac delta point measures and can be characterized as follows: At the highest level, the effective energy is entirely local; i.e., the energy focuses *separately* on the energy of each particle. At the next level, we see a Coulomb-like interaction between the particles. It is this latter part of the energy which we expect enforces a periodic array of masses. Proving this is a nontrivial matter: The closest related result we know is in [50].

There is a natural framework in which to rigorously establish these effective energies, that of Γ -convergence [6] in the space of measures equipped with the weak star topology. The details are too extensive to present here: They appear for the sharp interface functional (cf. (5.18) below) in [10] and are in preparation for the full functional [11]. However, it is relatively straightforward to formally capture these two levels of *effective* energies in the sharp interface limit. We present this in three dimensions.

Our starting point is the assumption that for η small, minimizers must have a basic structure of small separated particles (see Figure 10) which, after rescaling, tend to Dirac delta point measures. Recall that the energy has the form

$$(5.16) \quad E_{\varepsilon,\sigma}(u) := \frac{\varepsilon^2}{2} \int_{\Omega} |\nabla u|^2 dx + \int_{\Omega} W(u) dx + \frac{\sigma}{2} \|u - f_{\Omega} u\|_{H^{-1}}^2,$$

where $W(u) := (1 - u^2)^2/4$. We wish to consider the limiting behavior as both $\varepsilon \rightarrow 0$ and $m = f_{\Omega} u \rightarrow -1$ but the number of period cells remains $O(1)$. In order to capture something nontrivial in this limit—as the volume fraction m tends to -1 (f tends to 0) all the mass vanishes—we must pay careful attention to rescalings. To this end, let us not first a priori constrain the volume fraction of u . Rather let us perform a natural rescaling involving a limiting small parameter which will equivalently have the effect of sending the volume fraction to zero. To this end, we choose a new small parameter η and rescale as follows:

$$(5.17) \quad v := \frac{1}{2\eta}(u + 1), \quad \sigma = \frac{\varepsilon}{\eta}, \quad \widetilde{W}(v) := v^2(1 - \eta v)^2,$$

so that the wells of \widetilde{W} are at 0 and $1/\eta$, and the energy $E_{\varepsilon,\sigma}$ can be written as

$$E_{\varepsilon,\sigma}(u) = 2\varepsilon\eta E_{\varepsilon,\eta}(v) := 2\varepsilon\eta \left\{ \varepsilon\eta \int_{\Omega} |\nabla v|^2 + \frac{2\eta}{\varepsilon} \int_{\Omega} \widetilde{W}(v) + \|v - f_{\Omega} v\|_{H^{-1}}^2 \right\}.$$

The introduction of η and the above rescaling have the effect of naturally facilitating the convergence to a sum of delta point measures. Moreover, we may consider a limit where both

$$\eta \longrightarrow 0 \quad \text{and} \quad f = \frac{1}{2} \left(\int_{\Omega} u + 1 \right) \longrightarrow 0$$

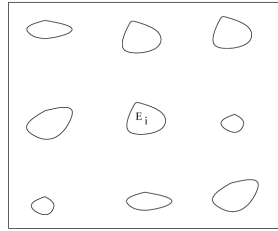


FIG. 10. Description of v_η representing an array of separated particles.

but with f/η fixed. This will allow for the extra degree of freedom that as $\eta \rightarrow \infty$, the distribution of mass f/η across the point measures may not be uniform.

As in section 5.2 we consider the strong segregation or sharp interface limit (corresponding to $\varepsilon \rightarrow 0$), in which

$$\varepsilon\eta \int_\Omega |\nabla v|^2 + \frac{2\eta}{\varepsilon} \int_\Omega \widetilde{W}(v) \approx c_0 \int_\Omega |\nabla v|,$$

provided $v \in \{0, 1/\eta\}$, with $c_0 = 2^{1/2} \int_0^1 W(s) ds$. This limit is rigorously justified by the well-known Modica–Mortola theorem of Γ -convergence (see, for example, [6]). This prompts the definition

$$(5.18) \quad F_\eta(v) := c_0 \int_\Omega |\nabla v| + \|v - f_\Omega v\|_{H^{-1}}^2, \quad \text{provided } v \in BV(\Omega, \{0, 1/\eta\}).$$

The argument of section 5.2 involving small spheres shows that the minimum energy of F_η scales like $\eta^{-1/3}$. Thus the energy tends to infinity as $\eta \rightarrow 0$ (note that the H^{-1} norm of a delta function is infinite in dimension $n = 3$). We now wish to investigate the asymptotics of the $\eta^{1/3} F_\eta(v)$ as $\eta \rightarrow 0$. We remark that this problem shares many common characteristics with the asymptotic analysis of the well-known *Ginzburg–Landau functional* which models magnetic vortices in superconductors [5, 2, 22].

The limiting behavior of the energy is best illustrated by studying a sequence v_η associated with a finite collection of disjoint particles. Let $v_\eta = \sum_{i=1}^{n_\eta} v_\eta^i$, where each v_η^i is of the form $v_\eta^i = \eta^{-1} \chi_{E_\eta^i}$, and the sets E_η^i are connected with a smooth boundary (see Figure 10). We define the mass of each connected component as

$$\alpha_\eta^i = \int_\Omega v_\eta^i = \frac{1}{\eta} |E_\eta^i|.$$

As $\eta \rightarrow 0$ we assume the following convergence (weak-* convergence in the sense of measures):

$$(5.19) \quad v_\eta \longrightarrow \sum_i \alpha^i \delta_{x^i}, \quad \text{where } \alpha_\eta^i \rightarrow \alpha^i \text{ and } x^i \in \Omega.$$

By adding a constant we can assume that G is the Green’s function for $-\Delta$ on the torus Ω satisfying

$$\int_\Omega G(x, y) dy = 0 \quad \forall x \in \Omega,$$

so that we find the simpler form

$$\|v - f_\Omega v\|_{H^{-1}}^2 = \int_\Omega \int_\Omega G(x, y) v(x) v(y) dx dy.$$

Note that G is bounded from below. The energy $F_\eta(v_\eta)$ of (5.18) then splits into two pieces:

$$\begin{aligned}
 \eta^{1/3} F_\eta(v_\eta) &= \eta^{1/3} \sum_i \left\{ c_0 \int_\Omega |\nabla v_\eta^i| + \int_\Omega \int_\Omega G(x, y) v_\eta^i(x) v_\eta^i(y) dx dy \right\} \\
 &\quad + \eta^{1/3} \sum_{(i,j): i \neq j} \int_\Omega \int_\Omega G(x, y) v_\eta^i(x) v_\eta^j(y) dx dy \\
 &= \eta^{1/3} \sum_i F_\eta(v_\eta^i) \\
 (5.20) \quad &\quad + \eta^{1/3} \sum_{(i,j): i \neq j} \int_\Omega \int_\Omega G(x, y) v_\eta^i(x) v_\eta^j(y) dx dy.
 \end{aligned}$$

As η tends to zero, the second term vanishes, since by (5.19)

$$\sum_{(i,j): i \neq j} \int_\Omega \int_\Omega G(x, y) v_\eta^i(x) v_\eta^j(y) dx dy \longrightarrow \sum_{(i,j): i \neq j} \alpha^i \alpha^j G(x^i, x^j).$$

The first term in (5.20) is $O(1)$ as $\eta \rightarrow 0$ and is essentially the sum of the energies of each of the particles; i.e., there is no interaction between the blobs, and thus the leading-order behavior is entirely local. Hence as η tends to zero, we expect an effective energy defined over weighted Dirac point measures which will see only the limiting mass factor α^i . In fact, it will be a sum of individual energies, consisting of the perimeter and the H^{-1} norm (now defined over all of \mathbb{R}^3), which are defined for characteristic functions of mass α^i .

On the other hand, (5.20) and (5.19) suggest that if one subtracts this first-order effective energy from $\eta^{1/3} F_\eta(v_\eta)$, divides the difference by $\eta^{1/3}$, and lets η tend to 0, the result converges to a Coulomb-like interaction energy over all distinct pairs of the points x^i , i.e., an effective energy of the form

$$\sum_{(i,j): i \neq j} \alpha^i \alpha^j G(x^i, x^j),$$

defined over point measures $\sum_i \alpha^i \delta_{x^i}$. As we have said, these statements are made precise in the context of Γ -convergence in [10].

5.4. Two related works. We briefly discuss here two recent and related works concerning minimizers of (2.2) in Region III. In [36] Ren and Wei prove the existence of sphere-like solutions to the Euler–Lagrange equation of (2.2) and further investigate their stability. The regimes for which these solutions exist overlap with Region III. They also show that the centers of sphere-like solutions are close to global minimizers of an effective energy defined over point masses which includes both a local energy defined over each mass and a Green’s function interaction term which sets the location of the approximate spheres. Thus while the nature of their result and methods used are different from ours, their results are in the same spirit.

In [17], Glasner and the first author explore the dynamics of small spherical phases for a gradient flow of the sharp interface version of (2.2) with small volume fraction. Here one finds, confirmed by simulations of (2.6), that there is a separation of time

scales for the dynamics: Small particles both exchange material as in usual Ostwald ripening and migrate because of an effectively repulsive nonlocal energetic term. Coarsening via mass diffusion occurs only while particle radii are small, and they eventually approach a finite equilibrium size. Migration, on the other hand, is responsible for producing self-organized patterns. By constructing approximations based upon an ansatz of spherical particles similar to the classical LSW (Lifshitz–Slyozov–Wagner) theory, one derives a finite-dimensional dynamics for particle positions and radii. For large systems, kinetic-type equations which describe the evolution of a probability density are constructed. A separation of time scales between particle growth and migration allows for a variational characterization of spatially inhomogeneous quasi-equilibrium states.

Heuristically this matches our findings of (a) a first-order energy which is local and essentially driven by perimeter reduction, and (b) a Coulomb-like interaction energy, at the next level, responsible for placement and self-organization of the pattern. It would be interesting if one could make these statements precise via the calculation of gradient flows and their connection with Γ -convergence [39].

6. Discussion. We have made a preliminary study of characterizing minimizers of (2.2) throughout the $m \times \gamma$ plane. In doing so, we have laid the foundation for a very rich variational problem based upon a physical problem of contemporary interest. Besides numerical simulations, Region I is the only region wherein a complete characterization of the ground state is possible. Region III allows for an energetic asymptotic analysis which will be complemented with rigorous Γ -convergence results (cf. [10] and [11]). These results give not only rigorous support to sphere-like global minimizers in an asymptotic regime of the phase plane but also give a decomposition of the relative effects of the different terms in the energy. They are also very much in the same spirit as recent work on the asymptotics of the Ginzburg–Landau energy and the structure of magnetic vortices in Type-II superconductors.

However mathematically interesting and attractive, these asymptotic results will not yield any precise information for particular (finite) values of m and γ . Thus for the purposes of the phase diagram, our primary tool will continue to be numerical simulations. Formal asymptotics for the bifurcation of lamellar and spherical phases is in preparation, and this will help in the numerical creation of a full phase diagram which can be compared with the SCMFT and experimental diagrams of Figure 2. Note that we have already been able to simulate all but one (the $Fddd$ phase) of the phases observed in the experimental phase diagram. This included the perforated lamellar phase which was not seen as a stable (globally minimizing) phase in the SCMFT calculations.

Although the numerical experiments show the boundary between Regions III and IV begins at $\gamma > 2$ we believe that this curve actually emerges from $(0, 2)$. In fact, preliminary formal asymptotics suggest that all boundary curves emerge from this point. A more detailed analysis of this is forthcoming. Moreover, based upon numerical simulations, we also believe that it is this curve which is the true ODT curve; that is, below this curve the uniform state is the unique global minimizer, and hence Region I and IV, are, in effect, one region. Numerical experiments in Region III are consistent with the analysis we presented in sections 5.2 and 5.3, suggesting minimizers are spherical. Note that this spherical regime extends into Region II.

One might be tempted, at this stage, to extrapolate from Figure 7 and include a preliminary sketch of the full phase diagram, qualitatively comparable to the SCMFT diagram of Figure 2. We resist this temptation: A detailed numerical phase diagram

is in progress wherein many more runs will be performed to far greater resolution and wherein we include a detailed geometrical analysis of the level sets of the steady states. Moreover, via (2.4), (2.5), and a certain calibration of constants, we will hopefully be able to compare, close to the order-disorder transition, our results with the SCMFT and the experimental results of Figure 2.

Finally we note that with the exception of Theorem 3.1, our focus has been on the physically relevant spatial dimension $n = 3$. Mathematically, it is natural to ask about the phase diagram of (2.2) in other dimensions, especially as the nature of the Green's function for the third term is highly sensitive to the dimension. In dimension $n = 1$, essentially one has a full understanding of the phase diagram, with the only structure phases being periodic (cf. [27, 31]). In dimension $n = 2$, whereas the range of possible minimizers is quite small (lamellae and periodic arrays of disks are the natural candidates), we are again faced with the fact that very little is rigorously known about global minimizers—there has certainly been much work on local minimizers and the stability of the basic candidate structures, e.g., [32, 34, 7]. For Region III, we carry out the same asymptotic investigation in two dimensions in [10, 11]. Here we see some fundamental differences with respect to three dimensions which are reflected in both the scalings of the reduced functionals (cf. (5.18)) and the effective first- and second-order energies. Numerically, two dimensions present an interesting test case for overcoming metastability issues and directly simulating both the spherical (disks) and lamellar phase in their respective positions of the phase plane starting with random initial conditions. The metastability issues alluded to in section 4.3 are also present in two dimensions. Hence for a full evaluation of parameter space, direct simulation of (2.6) is insufficient, as one will often get stuck in a metastable state which certainly has larger energy than the global (and perhaps many local) minimizers. Approaches based upon *artificially* driving the evolution out of undesired metastable states are needed, and (2.6) in two dimensions provides a good test case for such methods. Any method to do this is physically reasonable, as the temporal dynamics of the PDE are not of primary interest. Rather, we are foremost interested in the stationary states which minimize (1.1). Once efficient and reliable methods to do this have been developed for two dimensions we will be able to perform the detailed phase diagram in three dimensions.

Appendix A. Details of the numerical simulations. All computations were performed in MATLAB using both fourth-order exponential time differencing Runge–Kutta (ETDRK) [24] and a pseudospectral spatial discretization. Sample codes are available at <http://www.math.sfu.ca/~jfwillia>. Periodic boundary conditions were imposed and initial data was typically defined by $u_i = r_i + m$, $i = 1, \dots, N^n$, with r_i selected uniformly from the interval $(-1 - m, 1 - m)$ with mean zero. This initial data was then evolved until $\|u_t\| < \text{TOL}_1$ or $E(u(\cdot, t)) < E(m) - \text{TOL}_2$ for specified tolerances. Although steady state was not reached if only the second condition was met, we are certain that the solution has evolved to a lower energy state than the disordered profile $u \equiv m$.

A test of the two-dimensional code was performed by randomly sampling values of (m, γ) from $(0, 1) \times (2, 20)$ and taking initial data as $m + r$ with r randomly drawn from the uniform distribution on $(-.2, .2)$. The data was evolved until either

$$\max(u(\cdot, t)) - \min(u(\cdot, t)) < .001 \quad \text{or} \quad \|u_t\| < .0001.$$

The results of the experiment are presented in Figure 11. These results clearly demonstrate that the method respects the linear stability of the disordered state. Also the

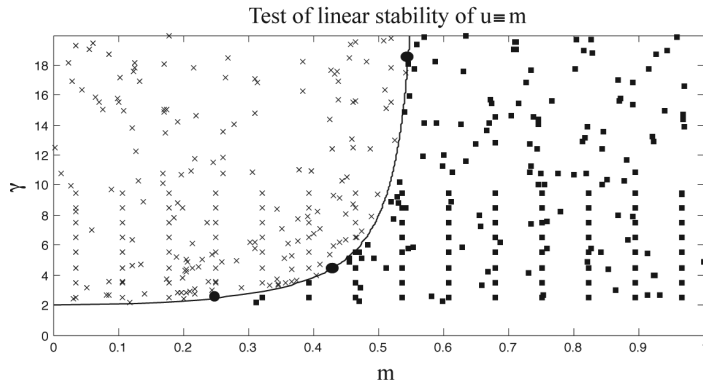


FIG. 11. *Linear stability of $u \equiv m$. The \times 's mark solutions where $\max(u(\cdot, t_{final})) - \min(u(\cdot, t_{final})) > .001$ and the \square 's where $\max(u(\cdot, t_{final})) - \min(u(\cdot, t_{final})) < .001$. The solid line is $\gamma = \frac{2}{1-3m^2}$ at which the linear stability of the disordered state changes. The three circles mark those runs which were categorized incorrectly using these tolerances. All three of these cases are very close to the stability curve and can be attributed to the numerical accuracy of the method and the tolerances.*

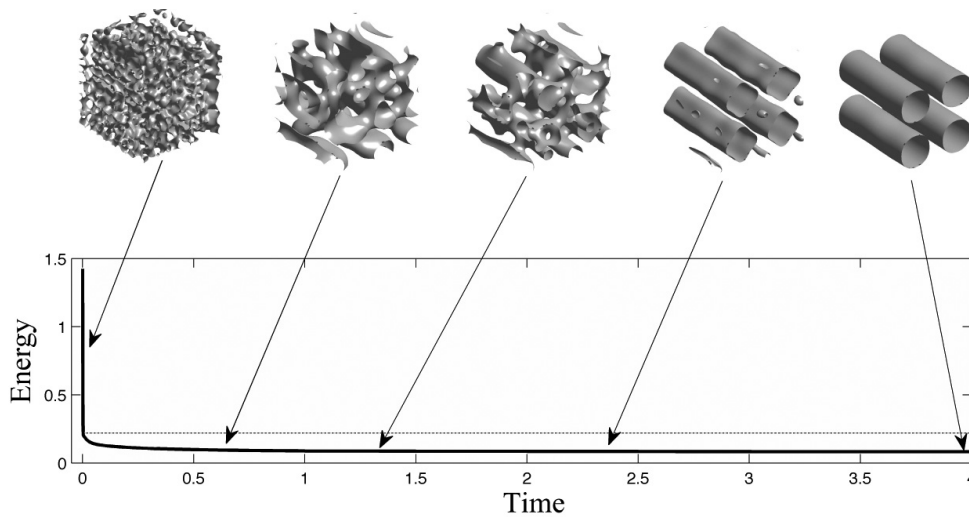


FIG. 12. *Typical energy decay. $\Omega = [-\pi/4, \pi/4]^3$, $\varepsilon = .04$, $\gamma = 25$, and $m = 0.35$. It is important to note that while the solution changed significantly over the entire time interval, the energy hardly changed at all after an initial transient.*

code decreases the energy (Figure 12).

Appendix B. The H^{-1} norm. Let Ω denote the three-dimensional flat torus of unit volume. Consider the Hilbert space

$$H := \left\{ f \in L^2(\Omega) \mid \int_{\Omega} f \, dx = 0 \right\},$$

equipped with the following inner product. For $f, \tilde{f} \in H$, let v, \tilde{v} denote the functions in H satisfying

$$-\Delta v = f \quad \text{and} \quad -\Delta \tilde{v} = \tilde{f} \quad \text{on } \Omega,$$

and define

$$\langle f, \tilde{f} \rangle_H := \int_{\Omega} \nabla v \cdot \nabla \tilde{v} \, dx.$$

Thus the norm in H is

$$(B.21) \quad \|f\|_H^2 = \int_{\Omega} |\nabla v|^2.$$

In Fourier space, denoting the \mathbf{k} th Fourier coefficient of f by $\hat{u}(\mathbf{k})$, we have

$$\|f\|_H^2 = \sum_{|\mathbf{k}| \neq 0} \frac{|\hat{u}(\mathbf{k})|^2}{|2\pi\mathbf{k}|^2}.$$

The norm (B.21) is also the norm of the *dual space* of H_0^1 (the functions in H^1 with zero average) with respect to the standard pairing. That is, letting $C_0^\infty(\Omega)$ denote the space of C^∞ functions on the torus Ω with zero average,

$$\|f\|_H^2 = \sup_{\psi \in C_0^\infty(\Omega)} \frac{(\int_{\mathbb{T}^n} f \psi)^2}{\|\nabla \psi\|_{L^2(\Omega)}^2}.$$

Whereas it has become standard folklore that the Cahn–Hilliard equation can be interpreted as a *gradient flow with respect to H^{-1}* , this is surprisingly written down in very few places (e.g., the notes of Fife [15]). Since this calculation is rather straightforward, let us show how to derive (2.6) as a gradient flow of (2.2) with respect to the H inner product. To this end, let us assume all functions are smooth (including ones in H). Let $\delta > 0$. We define $\text{grad}_H E_{\varepsilon, \sigma}(u)$ to be an element of H such that for all

$$W(t) : [0, \delta] \rightarrow H,$$

with $W(0) = u$, we have

$$\left. \frac{d}{dt} E_{\varepsilon, \sigma}(W(t)) \right|_{t=0} = \left\langle \text{grad}_H E_{\varepsilon, \sigma}(u), \left. \frac{\partial W}{\partial t} \right|_{t=0} \right\rangle_H.$$

In particular, for any $w \in H$, we have

$$\left. \frac{d}{dt} E_{\varepsilon, \sigma}(u + tw) \right|_{t=0} = \langle \text{grad}_H E_{\varepsilon, \sigma}(u), w \rangle_H.$$

Thus if $u(x, t)$ follows the flow

$$(B.22) \quad u_t = -\text{grad}_H E_{\varepsilon, \sigma}(u),$$

we have

$$\left. \frac{d}{dt} E_{\varepsilon, \sigma}(u(x, t)) \right|_{t=0} = \left\langle \text{grad}_H E_{\varepsilon, \sigma}(u), \left. \frac{\partial u}{\partial t} \right|_{t=0} \right\rangle_H = -\|\text{grad}_H E_{\varepsilon, \sigma}(u)\|_H^2 \leq 0.$$

Let us compute $\text{grad}_H E_{\varepsilon, \sigma}(u) \in H$. To this end, let u be such that $\int_{\Omega} u = m$. We compute the gradient with respect to parallel space $u + H$. Thus for $w \in H$ and $t \in [0, \delta]$, consider for $u + tw$, and let $v, \tilde{v} \in H$ solve

$$-\Delta v = u - m \quad \text{and} \quad -\Delta \tilde{v} = w \quad \text{in } \Omega.$$

We find

$$\begin{aligned} \left. \frac{d}{dt} E_{\varepsilon, \sigma}(u + tw) \right|_{t=0} &= \int_{\Omega} (u^3 - u - \varepsilon^2 \Delta u) w + \sigma \nabla v \cdot \nabla \tilde{v} \, dx \\ &= \int_{\Omega} (u^3 - u - \varepsilon^2 \Delta u) (-\Delta \tilde{v}) + \sigma \nabla v \cdot \nabla \tilde{v} \, dx \\ &= \int_{\Omega} \nabla (-\varepsilon^2 \Delta u - u + u^3 + \sigma v) \cdot \nabla \tilde{v} \, dx \\ &= \left\langle -\Delta (-\varepsilon^2 \Delta u - u + u^3 + \sigma v), w \right\rangle_H. \end{aligned}$$

Thus

$$\begin{aligned} \text{grad}_H E_{\varepsilon, \sigma}(u) &= -\Delta (-\varepsilon^2 \Delta u - u + u^3 + \sigma v) \\ &= -\Delta (-\varepsilon^2 \Delta u - u + u^3) + \sigma(u - m), \end{aligned}$$

and (B.22) gives

$$\frac{\partial u}{\partial t} = \Delta (-\varepsilon^2 \Delta u - u + u^3) - \sigma(u - m).$$

For completeness, we supply a proof of Proposition 5.1 which is similar to the result for the $H^{-1/2}$ norm presented in [9].

Proof of Proposition 5.1. We adopt the standard notion of using $f \lesssim g$ and $f \cong g$ to denote, respectively, $f \leq Cg$ and $f = Cg$ for some constant C . Without loss of generality we may rescale g to take values 0 and 1 instead of -1 and 1, respectively. Let

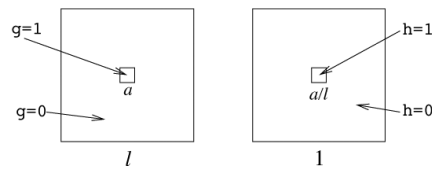
$$\hat{g}(\mathbf{k}) = \int_{[0, l]^3} g(x) e^{-2\pi i \frac{x \cdot \mathbf{k}}{l}}$$

denote the \mathbf{k} th Fourier coefficient of $g(x)$ on $[0, l]^3$. Let $h(x) = g(lx)$ and $\alpha = a/l$ (see Figure 13), and let $\hat{h}(\mathbf{k})$ be the Fourier coefficients of $h(x)$ on $[0, 1]^3$, i.e., with respect to the basis $e^{2\pi i x \cdot \mathbf{k}}$. We have

$$\hat{g}(\mathbf{k}) = l^3 \hat{h}(\mathbf{k}).$$

Focusing on $\hat{h}(\mathbf{k})$, we have (by a convenient translation within $[0, 1]^3$)

$$\begin{aligned} |\hat{h}(\mathbf{k})|^2 &\cong \left| \int_0^\alpha e^{-2\pi i k_1 x} dx \right|^2 \left| \int_0^\alpha e^{-2\pi i k_2 y} dy \right|^2 \left| \int_0^\alpha e^{-2\pi i k_3 z} dz \right|^2 \\ &\cong \frac{1}{k_1^2} |e^{-2\pi i k_1 \alpha} - 1|^2 \frac{1}{k_2^2} |e^{-2\pi i k_2 \alpha} - 1|^2 \frac{1}{k_3^2} |e^{-2\pi i k_3 \alpha} - 1|^2 \\ &= \frac{\sin^2 \pi k_1 \alpha}{k_1^2} \frac{\sin^2 \pi k_2 \alpha}{k_2^2} \frac{\sin^2 \pi k_3 \alpha}{k_3^2} \\ &\lesssim \frac{\alpha^2}{1 + \alpha^2 k_1^2} \frac{\alpha^2}{1 + \alpha^2 k_2^2} \frac{\alpha^2}{1 + \alpha^2 k_3^2}. \end{aligned}$$

FIG. 13. Rescaled versions of functions g and h in the proof of Proposition 5.1.

Thus

$$\begin{aligned}
 & \left\| g - \int_{[0,l]^3} g \right\|_{H^{-1}([0,l]^3)}^2 \\
 & \cong \sum_{|\mathbf{k}| \neq 0} \frac{|\widehat{g}(\mathbf{k})|^2}{l|\mathbf{k}|^2} \\
 & = l^5 \sum_{|\mathbf{k}| \neq 0} \frac{|\widehat{h}(\mathbf{k})|^2}{|\mathbf{k}|^2} \\
 & \lesssim l^5 \sum_{|\mathbf{k}| \neq 0} \frac{1}{|\mathbf{k}|^2} \frac{\alpha^2}{1 + \alpha^2 k_1^2} \frac{\alpha^2}{1 + \alpha^2 k_2^2} \frac{\alpha^2}{1 + \alpha^2 k_3^2} \\
 & \lesssim l^5 \int_0^\infty \int_0^\infty \int_0^\infty \frac{1}{\sqrt{x_1^2 + x_2^2 + x_3^2}} \frac{\alpha^2}{1 + \alpha^2 x_1^2} \frac{\alpha^2}{1 + \alpha^2 x_2^2} \frac{\alpha^2}{1 + \alpha^2 x_3^2} dx_1 dx_2 dx_3 \\
 & \lesssim l^5 \alpha^5 \int_0^\infty \int_0^\infty \int_0^\infty \frac{1}{\sqrt{x_1^2 + x_2^2 + x_3^2}} \frac{1}{1 + x_1^2} \frac{1}{1 + x_2^2} \frac{1}{1 + x_3^2} dx_1 dx_2 dx_3 \\
 & \lesssim a^5. \quad \square
 \end{aligned}$$

Acknowledgment. We would like to thank Mirjana Maras for help with the numerical experiments. Her MSc thesis at Simon Fraser includes a full two-dimensional phase diagram for (1.1), with a supporting asymptotic analysis.

REFERENCES

- [1] A. AKSIMENTIEV, M. FIALKOWSKI, AND R. HOLYST, *Morphology of surfaces in mesoscopic polymers, surfactants, electrons, or reaction-diffusion systems: Methods, simulations, and measurements*, Adv. Chem. Phys., 121 (2002), pp. 141–239.
- [2] G. ALBERTI, S. BALDO, AND G. ORLANDI, *Variational convergence for functionals of Ginzburg-Landau type*, Indiana Univ. Math. J., 54 (2005), pp. 1411–1472.
- [3] G. ALBERTI, R. CHOKSI, AND F. OTTO, *Uniform energy distribution for minimizers of an isoperimetric problem with long-range interactions*, J. Amer. Math. Soc., 22 (2009), pp. 569–605.
- [4] F. S. BATES AND G. H. FREDRICKSON, *Block copolymers—designer soft materials*, Physics Today, 52 (1999), pp. 32–38.
- [5] F. BETHUEL, H. BREZIS, AND F. HELEIN, *Ginzburg-Landau Vortices*, Progr. Nonlinear Differential Equations Appl. 13, Birkhäuser Boston, Boston, MA, 1994.
- [6] A. BRAIDES, *Γ -Convergence for Beginners*, Oxford Lecture Ser. Math. Appl., 22, Oxford University Press, Oxford, UK, 2002.

- [7] X. CHEN AND Y. OSHITA, *An application of the modular function in nonlocal variational problems*, Arch. Ration. Mech. Anal., 186 (2007), pp. 109–132.
- [8] R. CHOKSI, *Scaling laws in microphase separation of diblock copolymers*, J. Nonlinear Sci., 11 (2001), pp. 223–236.
- [9] R. CHOKSI, R. V. KOHN, AND F. OTTO, *Energy minimization and flux domain structure in the intermediate state of a Type-I superconductor*, J. Nonlinear Sci., 14 (2004), pp. 119–171.
- [10] R. CHOKSI AND M. A. PELETIER, *Small Volume Fraction Limit of the Diblock Copolymer Problem I: Sharp Interface Functional*, preprint, 2009.
- [11] R. CHOKSI AND M. A. PELETIER, *Small Volume Fraction Limit of the Diblock Copolymer Problem II: Diffuse Interface Functional*, in preparation.
- [12] R. CHOKSI AND X. REN, *On a derivation of a density functional theory for microphase separation of diblock copolymers*, J. Statist. Phys., 113 (2003), pp. 151–176.
- [13] R. CHOKSI AND P. STERNBERG, *Periodic phase separation: The periodic isoperimetric and Cahn-Hilliard problems*, Interfaces Free Bound., 8 (2006), pp. 371–392.
- [14] R. CHOKSI AND P. STERNBERG, *On the first and second variations of a nonlocal isoperimetric problem*, J. Reine Angew. Math., 611 (2007), pp. 75–108.
- [15] P. FIFE, *Models for phase separation and their mathematics*, Electron. J. Differential Equations, no. 48 (2000), pp. 1–26.
- [16] G. H. FREDRICKSON, *The Equilibrium Theory of Inhomogeneous Polymers*, Oxford University Press, Clarendon Press, Oxford, UK, 2006.
- [17] K. GLASNER AND R. CHOKSI, *Coarsening and self-organization in dilute diblock copolymer melts and mixtures*, Phys. D, submitted.
- [18] K. GROSSE-BRAUCKMANN, *Gyroids of constant mean curvature*, Experiment. Math., 6 (1997), pp. 33–50.
- [19] K. GROSSE-BRAUCKMANN, *On gyroid interfaces*, J. Colloid Interface Sci., 187 (1997), pp. 418–428.
- [20] K. GROSSE-BRAUCKMANN AND M. WOHLGEMUTH, *The gyroid is embedded and has constant mean curvature*, Calc. Var. Partial Differential Equations, 4 (1996), pp. 499–523.
- [21] I. W. HAMLEY, *The Physics of Block Copolymers*, Oxford University Press, Oxford, UK, 1998.
- [22] R. L. JERRARD AND H. M. SONER, *The Jacobian and the Ginzburg-Landau energy*, Calc. Var. Partial Differential Equations, 14 (2002), pp. 151–191.
- [23] H. KARCHER, *The triply periodic minimal surfaces of Alan Schoen and their constant mean curvature companions*, Manuscripta Math., 64 (1989), pp. 291–357.
- [24] A.-K. KASSAM AND L. N. TREFETHEN, *Fourth-order time-stepping for stiff PDEs*, SIAM J. Sci. Comput., 26 (2005), pp. 1214–1233.
- [25] A. K. KHANDPUR, S. FORSTER, F. S. BATES, I. W. HAMLEY, A. J. RYAN, W. BRAS, K. ALMDAL, AND K. MORTENSEN, *Polyisoprene-polystyrene diblock copolymer phase diagram near the order-disorder transition*, Macromolecules, 28 (1995), pp. 8796–8806.
- [26] M. W. MATSEN AND M. SCHICK, *Stable and unstable phases of a diblock copolymer melt*, Phys. Rev. Lett., 72 (1994), pp. 2660–2663.
- [27] S. MÜLLER, *Singular perturbations as a selection criterion for periodic minimizing sequences*, Calc. Var. Partial Differential Equations, 1 (1993), pp. 169–204.
- [28] Y. NISHIURA AND I. OHNISHI, *Some mathematical aspects of the micro-phase separation in diblock copolymers*, Phys. D, 84 (1995), pp. 31–39.
- [29] I. OHNISHI, Y. NISHIURA, M. IMAI, AND Y. MATSUSHITA, *Analytical solutions describing the phase separation driven by a free energy functional containing a long-range interaction term*, Chaos, 9 (1999), pp. 329–341.
- [30] T. OHTA AND K. KAWASAKI, *Equilibrium morphology of block copolymer melts*, Macromolecules, 19 (1986), pp. 2621–2632.
- [31] X. REN AND J. WEI, *On energy minimizers of the diblock copolymer problem*, Interfaces Free Bound., 5 (2003), pp. 193–238.
- [32] X. REN AND J. WEI, *Stability of spot and ring solutions of the Diblock copolymer equation*, J. Math. Phys., 45 (2004), pp. 4106–4133.
- [33] X. REN AND J. WEI, *Wriggled lamellar solutions and their stability in the diblock copolymer problem*, SIAM J. Math. Anal., 37 (2005), pp. 455–489.
- [34] X. REN AND J. WEI, *Droplet solutions in the diblock copolymer problem with skewed monomer composition*, Calc. Var. Partial Differential Equations, 25 (2006), pp. 333–359.
- [35] X. REN AND J. WEI, *Existence and stability of spherically layered solutions of the diblock copolymer equation*, SIAM J. Appl. Math., 66 (2006), pp. 1080–1099.
- [36] X. REN AND J. WEI, *Spherical solutions to a nonlocal free boundary problem from diblock copolymer morphology*, SIAM J. Math. Anal., 39 (2008), pp. 1497–1535.
- [37] A. ROS, *The isoperimetric problem*, in Global Theory of Minimal Surfaces, AMS, Providence,

- RI, 2005, pp. 175–209.
- [38] A. ROS, *Stable periodic constant mean curvature surfaces and mesoscopic phase separation*, *Interfaces Free Bound.*, 9 (2007), pp. 355–365.
- [39] E. SANDIER AND S. SERFATY, Γ -convergence of gradient flows with applications to Ginzburg-Landau, *Comm. Pure Appl. Math.*, 57 (2004), pp. 1627–1672.
- [40] M. F. SCHULZ, A. K. KHANDPUR, F. S. BATES, K. ALMDAL, K. MORTENSEN, D. A. HAJDUK, AND S. M. GRUNER, *Phase behavior of polystyrene-poly(2-vinylpyridine) diblock copolymers*, *Macromolecules*, 29 (1996), pp. 2857–2867.
- [41] M. SEUL AND D. ANDELMAN, *Domain shapes and patterns: The phenomenology of modulated phases*, *Science*, 267 (1995), pp. 476–483.
- [42] A.-C. SHI, *Self-consistent field theory of block copolymers*, in *Developments in Block Copolymer Science and Technology*, I. W. Hamley, ed., Wiley, Chichester, 2004, pp. 265–294.
- [43] E. N. SPADARO, *Uniform energy and density distribution: Diblock copolymer functional*, *Interfaces Free Bound.*, to appear.
- [44] X. SUN AND M. J. WARD, *Dynamics and coarsening of interfaces for the viscous Cahn-Hilliard equation in one spatial dimension*, *Stud. Appl. Math.*, 105 (2000), pp. 203–234.
- [45] M. TAKENAKA, T. WAKADA, S. AKASAKA, S. NISHITSUJI, K. SAIJO, H. SHIMIZU, M. I. KIM, AND H. HASEGAWA, *Orthorhombic Fddd network in diblock copolymer melts*, *Macromolecules*, 40 (2007), pp. 4399–4402.
- [46] T. TERAMOTO, M. GAMEIRO, AND Y. NISHIURA, *Applications of Computational Homology to 3D Morphology Transitions*, preprint, 2008.
- [47] T. TERAMOTO AND Y. NISHIURA, *Double gyroid morphology in a gradient system with nonlocal effects*, *J. Phys. Soc. Japan*, 71 (2002), pp. 1611–1614.
- [48] T. TERAMOTO AND Y. NISHIURA, *Double gyroid morphology of the diblock copolymer problem*, *RIMS Kokyuroku*, 1356 (2004), pp. 116–121.
- [49] *The Scientific Graphics Project, MSRI, Berkeley*, <http://www.msri.org/about/sgp/SGP/index.html>
- [50] F. THEIL, *A proof of crystallization in two dimensions*, *Comm. Math. Phys.*, 262 (2006), pp. 209–236.
- [51] E. THOMAS, D. M. ANDERSON, C. S. HENKEE, AND D. HOFFMAN, *Periodic area-minimizing surfaces in block copolymers*, *Nature*, 334 (1988), pp. 598–601.
- [52] C. A. TYLER AND D. C. MORSE, *Orthorhombic Fddd network in triblock and diblock copolymer melts*, *Phys. Rev. Lett.*, 94 (2005), 208301.
- [53] K. YAMADA, M. NONOMURA, AND T. OHTA, *Fddd structure in AB-type diblock copolymers*, *J. Phys.: Condens. Matter*, 18 (2006), pp. L421–L427.
- [54] K. YAMADA AND T. OHTA, *Interface between lamellar and gyroid structures in diblock copolymer melts*, *J. Phys. Soc. Japan*, 76 (2007), 084801.